



Non-reciprocity and exchange-spring delay of domain-wall Walker breakdown in magnetic nanowires with azimuthal magnetization

Lucía Gómez-Cruz ^{1,2} Laura Álvaro-Gómez ¹ Claudia Fernández-González ³ Sandra Ruiz-Gómez ³ Christophe Thirion ⁴ Giuseppe Curci ⁵ Lucia Aballe ³ Eva Pereiro ³ Rachid Belkhou ⁶ Eduardo Martínez ⁴ Victor Raposo ⁴ Jean-Christophe Toussaint ⁴ Daria Guskova ⁵ Aurélien Masseboeuf ⁵ Olivier Fruchart ⁵ and Lucas Pérez ^{1,7}

¹*Dpto. Física de Materiales, Universidad Complutense de Madrid, Plaza de las Ciencias 1, Madrid, 28040, Spain*

²*Univ. Grenoble Alpes, CNRS, CEA, SPINTEC, Grenoble INP, 38000 Grenoble, France.*

³*Alba Synchrotron Light Facility, CELLS, Carrer de la Llum 2-26, Cerdanyola del Vallès, 08290, Barcelona, Spain*

⁴*Univ. Grenoble Alpes, CNRS, Institut Néel, 38000 Grenoble, France*

⁵*Univ. Grenoble Alpes, CNRS, CEA, SPINTEC, 38000 Grenoble, France.*

⁶*Synchrotron SOLEIL, Saint-Aubin, F-91192 Gif-sur-Yvette, France*

⁷*Instituto Madrileño de Estudios Avanzados - IMDEA Nanociencia, C/ Faraday 9, Madrid, 28049, Spain*

Domain-wall (DW) motion is a crucial process involved in magnetization reversal, be it under magnetic field or spin-polarized current stimulus. In most cases DW speed does not exceed ≈ 100 m/s and collapses above a given threshold of the stimulus, an effect known as Walker breakdown. A few specific material properties have been identified to delay the breakdown of speed by increasing the energy barrier preventing internal precession. We show that in a 3D nanomagnetic system, here with vortex-state domains, the topology of the magnetization distribution may intrinsically and robustly delay the Walker breakdown due to an exchange-spring effect. In addition, curvature induces a major non-reciprocal effect, delaying or not the Walker breakdown depending on the chirality of the azimuthal domain versus the direction of motion of the DW.

I. INTRODUCTION

The response of a system to an external driving force may be linear at small drive amplitude and enter a turbulent regime above a critical threshold. A typical example is fluid dynamics, transiting from laminar to turbulent flow for Reynolds numbers above a critical value, which depends on fluid inertia, system dimension, flow speed and viscosity. Domain wall (DW) motion in a magnetic material shows an analogous behavior, when set in motion by a magnetic field[1] or a spin-polarized current[2]: DWs usually display a constant mobility at low drive, and enter a turbulent regime above a so-called Walker breakdown field (resp., current). The underlying physics is very rich, involving the continuous precession of magnetization inside the DW and possibly the nucleation of sub-textures in the magnetization of the DW such as vortices. Besides fundamental interest, the understanding and control of DW motion is crucial to develop reliable and efficient applications in data storage and logic[3].

Flat strips are a textbook situation to investigate DW dynamics[4], owing to their nearly one-dimensional shape and thus limited number of degrees of freedom. The Walker breakdown generally limits speed to around 100 m/s experimentally, such as in the prototypical soft magnetic material Permalloy, under either magnetic field[5] or electric current[6, 7]. Some intrinsic material properties may delay the onset of DW precession, such as

the Dzyaloshinskii-Moriya interaction (DMI) promoting a given chirality of the DW[8], or the vanishing magnetization in compensated ferrimagnets[9, 10]. This, however, remains material-specific.

Three-dimensional (3D) magnetic systems have been receiving attention in the past decade[11–13], as their shape can induce a number of effects, adding to the material intrinsic properties: curvature-induced magnetic anisotropy or DMI, chirality, and/or topology constraints, *e.g.* the magnetic Möbius string preventing the existence of a uniform magnetic state[14]. As regards DW motion, cylindrical structures are the textbook counterpart of flat strips for 3D systems. In some of these systems it has been predicted that the enhanced strength of magnetostatic energy in 3D delays the Walker breakdown by increasing the energy barrier associated with DW precession. This concerns head-to-head DWs in both cylindrical wires[1, 15], the so-called Bloch DW, and in cylindrical nanotubes[16]. As a consequence, speeds exceeding 500 m/s have been predicted, with encouraging experimental reports[17, 18].

Here, we demonstrate a material-independent effect delaying the Walker breakdown, stemming from the topology of a three-dimension magnetization texture in cylindrical nanowires (NWs). We consider DWs separating opposite-azimuthally-magnetized domains in soft-magnetic NWs with a uniformly-axially-magnetized core, also called a vortex state[19, 20] (FIG. 1a). This original geometry allows us to set the DWs in motion by

the Oersted field arising from a charge current flowing through the wire. We evidenced speed exceeding 500 m/s, which we explain by a magnetic exchange-bias between the core and the DWs at the wire periphery, a phenomenon analogous to the one proposed for exchange-spring magnets[21–23]. Unlike DMI, whose energy barrier peaks for a π rotation of the DW but the system comes back to its ground state for 2π rotation of magnetization, here the core hinders further rotation and therefore causes a substantial modification and delay of the Walker phenomenon. Besides, due to the curvature of the wire surface this phenomenon is chiral, depending on the relative orientation of peripheral magnetization with respect to the direction of DW motion.

The manuscript is organized as follows. We first describe the preparation and static properties of the samples considered. We then report DW motion under nanosecond pulses of charge current, imaged using Transmission X-ray Microscopy (TXM) and ptychography combined with X-ray Magnetic Circular Dichroism (XMCD). We finally link the high DW speed measured with the three-dimensional topology of magnetization, with the help of both analytical modeling and micromagnetic simulation.

II. EXPERIMENTS

We fabricated 200 nm-diameter cylindrical NWs by template-assisted electrodeposition (FIG. 1). The NWs are made of Permalloy segments, *i.e.*, $\text{Fe}_{20}\text{Ni}_{80}$, separated by 40 nm-long chemical modulations of composition of $\text{Fe}_{70}\text{Ni}_{30}$. The template is dissolved and a diluted drop of wire-containing solution is let to dry on 40 nm-thick Si_3N_4 windows held by a frame of Si wafer, to allow for transmission microscopy. Two electric pads for current pulses injection were subsequently patterned with laser lithography. We used TXM for magnetic imaging, with energy tuned to the Fe L_3 absorption edge (FIG. 1d). XMCD images were computed as the normalized difference of transmission images with left and right polarizations, which highlights the magnetization component collinear to the X-ray beam, either parallel (light) or antiparallel (dark) (FIG. 1e)[24]. The dark/light contrast on opposite sides of the wire reveals an azimuthal component of magnetization at its periphery. Azimuthal magnetic domains curling around an axially-magnetized core had been reported already three decades ago in amorphous Co-rich magnetostrictive microwires[25], with typical diameters of several tens of μm , and presenting the so-called Giant Magneto-Impedance effect[26]. Recently, azimuthal peripheral magnetic domains have also been reported in Permalloy nanowires with diameter of a few hundreds of nanometers[19, 20]. While it was initially thought that azimuthal domains arise in the vicinity of chemical modulations, it is now recognized that homogeneous wires of sufficient diameter may host them, typically above 100 nm to 150 nm.

Hereafter, domains characterized by a light-top and dark-bottom contrast will be referred to as ($C+$), whose axial vector is parallel to \mathbf{z} , while the reverse will be labeled as ($C-$). The sign of the Oersted field resulting from the pulses of current will be labeled the same, so that positive (resp. negative) current pulses are expected to favor domains with right (resp. left) circulation.

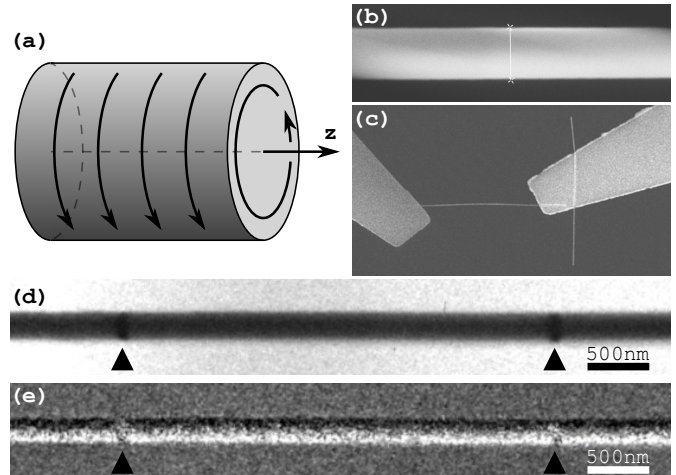


FIG. 1: (a) Sketch of a wire with azimuthal magnetization (b,c) SEM images of a 200 nm-diameter nanowire with Permalloy segments of average length 3.6 μm , separated with 40 nm-wide $\text{Fe}_{70}\text{Ni}_{30}$ chemical modulations: close-up and full view of an electrically-contacted nanowire. (d) Transmission and XMCD-TXM views of such NWs, with two consecutive chemical modulations highlighted with black triangular marks.

The bandwidth of the pulse generator, sample mounting and oscilloscope are limited to a few hundreds of MHz. Consequently, we cannot apply pulses of current shorter than 500 ps, and the varying current during the rise and fall times introduce a bias in the analysis (see End Matter). Therefore, in order to precisely infer the DW speed, we did not image a given DW after successive pulses, but instead we reset the sample circulation with a first current pulse and nucleate a fresh DW with an opposite pulse in a reproducible fashion between every two static images. The length of the second pulse can be adjusted finely, allowing us to monitor the DW displacement in intervals down to 100 ps, which is the nominal time resolution of our pulse generator. This approach also allows to disregard non-linear DW motion at the beginning and end of the pulses, such as inertia and threshold of current for motion. The way to define the pulse length is detailed in the End Matter section. The transmission image and the initial (reset) magnetic state are shown in FIG. 2(a). A ($C+$) domain is bonded by two domain walls pinned at the modulations. FIG. 2(b) shows the magnetic states resulting from the application of a pulse with amplitude $1.1 \times 10^{11} \text{ A}^2/\text{m}$ and increasing duration. The longer the pulse is, the further the

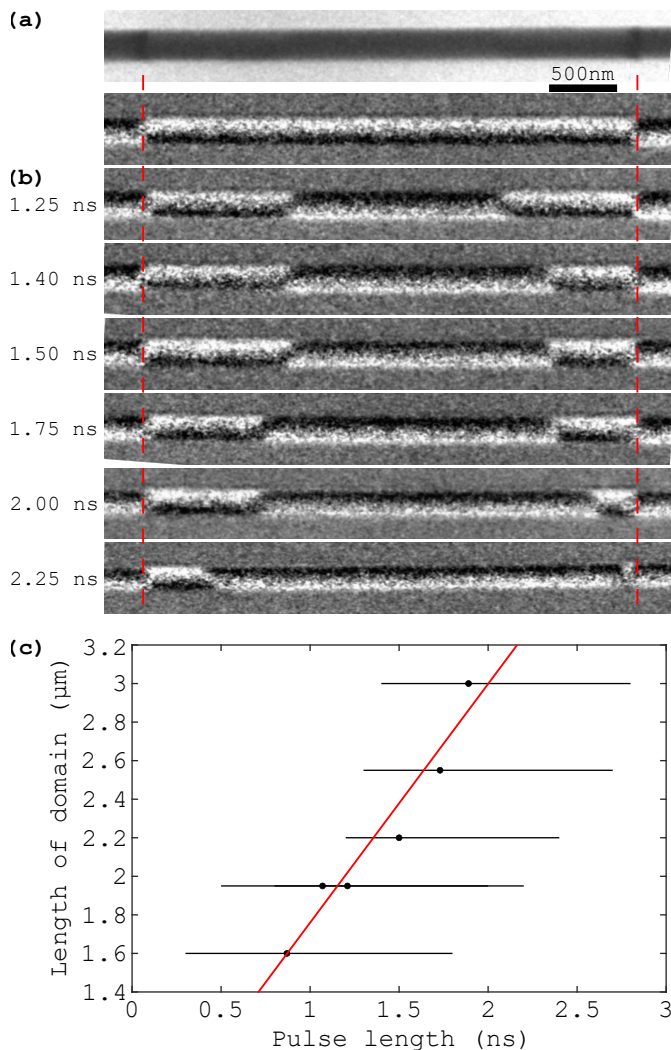


FIG. 2: (a) Transmission and XMCD image of the initial state. (b) Starting from the same initial state, each row is a static XMCD image taken after the application of a current pulse of $J = 1.1 \times 10^{11} \text{ A/m}^2$, with duration indicated on the left-hand side. After each step the initial state is recovered by applying a pulse with opposite polarity. The position of the chemical modulations is highlighted with vertical dashed red lines (c) Length of the nucleated domain versus the length of the current pulse. The horizontal lines are error bars (see End matter).

DWs have moved. This monotonous variation of DW position suggests that the nucleation site and process are reproducible, probably matching a specific chemical or structural defect in the nanowire. We estimate a temperature rise, due to Joule heating during a pulse, to be one degree or less (see End Matter). Thermal effects can thus be safely neglected.

FIG. 2(c) displays the length of the nucleated domain versus pulse length. The nucleation length is $\approx 500 \text{ nm}$, *i.e.*, extrapolated to null duration, with some uncer-

tainty due to the definition of pulse width and influence of DW inertia. The DW speed can be inferred to $v_{\text{DW}} \approx 600 \text{ m/s}$, averaging the speed of both DWs. This value comes with an uncertainty of the order of 100 m/s , owing to the error bars related to the control of pulse width, and possible stochastic DW pinning along the wire. Note that we could not investigate speed over an extensive range of applied current in the present wires. Indeed a lower bound of usable current is set by the critical value for nucleation. Conversely, for large current we have measured DW speeds up to 2 km/s . The latter values, however, had a large spread and depended on the pulse duration. Time-resolved imaging revealed that the mechanism is not DW motion but coherent switching of the circulation, occurring when the (Ersted field exceed the strength of azimuthal anisotropy (See End Matter). Consequently, we restrict our analysis to the current density $1.1 \times 10^{11} \text{ A/m}^2$, which corresponds to an (Ersted field with magnitude 7 mT at the periphery of the wire. This is of the order of the Walker field in thin films made of a soft-magnetic material, typically 2 mT to 3 mT , which however are limited to speed around 100 m/s . This suggests that a specific phenomenon delays the Walker breakdown in the present situation.

DW motion in microwires with azimuthal magnetization gives rise to Giant Magneto-Impedance in amorphous microwires at frequencies below those of ferromagnetic resonance, induced by the (Ersted field associated to the charge current flowing in the wire[25]. It can also induce the full switching of the circulation[27]. The switching of peripheral circulation was imaged directly [28], however only the speed of head-to-head domain walls arising on the wire axis was quantified[29]. Nanowires, with far fewer degrees of freedom, offer the opportunity to investigate physics down to its basic ingredients. It will also be shown that the much larger role of exchange in NWs plays a crucial role in DW motion.

III. ANALYSIS

FIG. 3a-c shows schematics of the simplest rotationally-invariant static DWs that one may consider for nanowires with azimuthal domains. FIG. 3a,b depict a Néel and a Bloch DW, respectively. In the former case the Néel component is parallel to magnetization on the axis, while FIG. 3c depicts a Néel wall antiparallel to magnetization on the axis. Note that the topology of the three walls is equivalent. In analogy with thin films, from a magnetostatic point of view Néel (resp. Bloch) walls could be expected to occur for small (resp. large) radius. However, another specific ingredient needs to be considered, namely, exchange coupling with magnetization on the axis. This adds an extra cost of exchange for the Bloch wall, compared to the Néel wall. Similarly, exchange is expected to lift the degeneracy between the two orientations of the Néel wall, due to the need to create a 180° twist with the axis

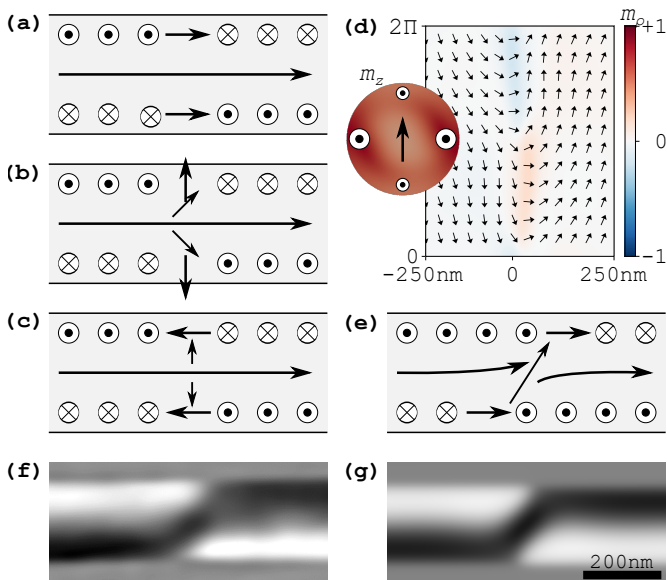


FIG. 3: Schematics for DWs. (a) Néel DW parallel to the axis, (b) Bloch DW (c) Néel DW antiparallel to the axis (d) Unrolled surface map, and cross section with sketches for the direction of magnetization, of a simulated DW (feeLLGood). The color codes the radial and longitudinal components of magnetization, respectively. (e) Schematics for (d). (f) Example of an experimental (ptychography) and (g) simulated transmission XMCD contrast of a DW of type (d-e).

for one orientation of them (FIG. 3c). Note that the states sketched in FIG. 3a-c are those expected to occur sequentially upon precession of the DW core around an (Ersted) field, such as would occur above a Walker breakdown. Therefore, precession comes at the expense of a continuously-increasing exchange field, reminiscent of an exchange-spring effect[21–23]. This is specific to the 3D rotationally-invariant situation, whose topology does not allow to unwind, unlike in the case of a thin film. A crude estimate for this radial exchange energy for the Néel wall in FIG. 3c, per unit of wall length along the wire periphery:

$$\mathcal{E}_{\text{ex}} = A \left(\frac{\pi}{R} \right)^2 R \delta \sim A \pi^2, \quad (1)$$

where A is the micromagnetic exchange stiffness, δ is the wall width, to first order assumed similar to the radius R [30]. Let us make the analogy with the Dzyaloshinskii-Moriya interaction lifting the degeneracy between the two directions of a Néel DW:

$$\mathcal{E}_{\text{DMI}} \approx \pi D_V R / 2, \quad (2)$$

with D_V the volume DMI coefficient. The comparison between Eq.(1) and 2 yields:

$$D_V \approx 2A\pi/R. \quad (3)$$

Applied to the typical values $A = 10^{-11}$ J/m and $R = 100$ nm, one gets $D_V = 0.6$ J/m², which is comparable to

the order of magnitude of the interfacial DMI measured in some ultrathin films[31]. Such an effective value of DMI is expected to enhance the Walker threshold and the maximum DW speed by up to one order of magnitude, under either magnetic field or spin-polarized current[8]. Besides, this simple analogy considers a twist of half a turn only, and neglects the magnetostatic energy arising from the twist, which would further stabilize the DW.

We conducted micromagnetic simulations to evaluate the situation more in depth. We used both feeLLGood[32] and MuMax[33] software, yielding similar results (see End Matter).

FIG. 3d shows the surface map and cross-section of a domain-wall at rest. It is similar to the Néel DW sketched in FIG. 3a, with two differences: first, there is a partial Bloch-type component of magnetization, *i.e.*, transverse to the wire, and radial and antiparallel on opposite sides of the wire; second, its intercepts with the wire surface are axially-shifted one with the other. This arrangement is similar to so-called asymmetric Néel walls in films with in-plane magnetization and intermediate thickness, with a mixed Bloch/Néel core and two Néel caps of the same orientation[34, 35] (FIG. 3e). We believe that this arrangement, breaking the rotational symmetry, allows to reduce the magnetostatic energy thanks to the Bloch component largely avoiding volume charges, the Néel caps avoiding surface charges, and globally minimizing exchange energy with the axis, as compared to the case in FIG. 3b. FIG. 3f,g show an experimental and simulated XMCD contrast of the DW, the latter computed from the simulated domain wall at rest[36], with blurring adjusted to match the experimental spatial resolution considered at the wire edges. The similarity between both suggests that the simulations describes accurately the experimental system.

We simulated the response of the DW to an applied current, considering the (Ersted) field as the sole driving force of motion[37], and covered damping coefficients in the range 0.01 to 0.1. For large damping and low current density the motion is steady-state, with speed 100 m/s or lower, which we will call regime I. Surface maps reveal only quantitative changes compared with FIG. 3d (not shown here).

For lower damping or larger current density, one or even two successive disruptions of DW motion occur over time, defining in total three regimes which we labeled I to III on FIG. 4a. Each disruption is associated with a qualitative transformation of the DW, as illustrated by their surface map and sketch of interior (FIG. 4c,d). It is consistent with the regime of DW motion below the Walker breakdown in the 1d model, *i.e.*, speed increases with applied current and decreases with damping. The transition to regime II occurs when the speed reaches approximately 200 m/s. Magnetization becomes fully radial at a given location, leading to the creation of a pair of surface vortex/antivortex pair that then move apart azimuthally. This dynamical process is analogous to others occurring for DWs in cylindrical nanowires under

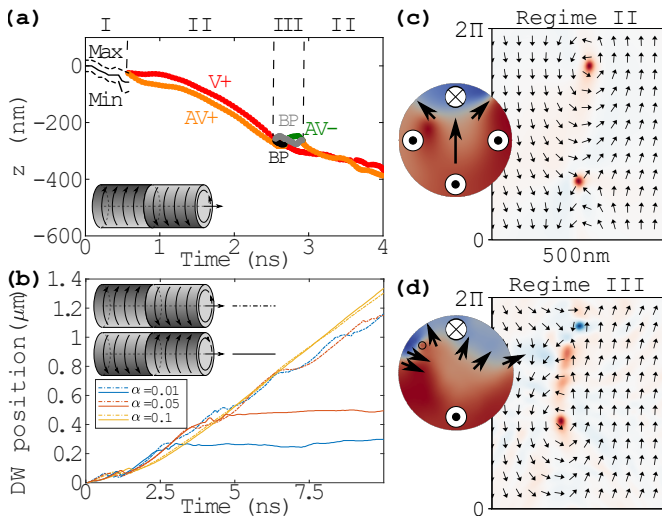


FIG. 4: Simulated DW motion. (a) Longitudinal position of DW versus time for $j = 10^{11} \text{ J/m}^2$ and $\alpha = 0.01$ (feeLLGood), with three regimes identified as I, II and III, and domains positive with respect to the DW propagation direction (inset). The graph displays the position of Min, average and Max of the radial component at the periphery for regime I, surface vortex (V)/antivortex (AV) along with their polarity in regime II, with addition Bloch points in regime III (b) DW displacement versus time for three values of damping and the two cases of circulation of domains on either side of the DW (MuMax) (c,d) Unrolled surface maps and cross sections for $j = 10^{11} \text{ J/m}^2$ and $\alpha = 0.01$, typical of regimes II and III from (a), at 1.841 ns and 2.842 ns, respectively, while regime I is qualitatively described by the static distribution shown in FIG. 3d with the same color scale (feeLLGood).

both applied field[38] or current[39, 40]. Magnetization in the peripheral area between the two surface objects has then rotated by π with respect to the DW at rest, *i.e.*, similar to the Néel wall shown in FIG. 3c. For intermediate values of current and damping the regime II reaches a steady state, invariant upon a combined translation/rotation. In this case, the process looks like the beginning of the precession of the internal degree of freedom of the DW, however reaching a dynamical equilibrium angle of 180° and not developing a full Walker process. For still lower damping or larger current density, a transition to regime III occurs for DW speed around 200 m/s, through the nucleation of a pair of Bloch and anti-Bloch points in the bulk of the wire (FIG. 3a). Shortly afterwards, the latter annihilates at the surface and thereby changing the polarity of the surface antivortex to negative (see Ref.40 for the conservation of the total topological charge). This process is analogous with the switching of vortex core during gyration, occurring around the same drift speed[41–43]. This process comes with a sharp drop of DW mobility, reminiscent of the Walker process in the 1d model[44]. However, in turn

and soon afterwards, the second Bloch point reaches the surface and switches the antivortex back to its initial positive polarity. The regime is again II, and the speed of the DW increases again. Thus, a Walker-like process with a 360° rotation of magnetization occurs in regime III but does not affect the entire DW, remaining close to the wire periphery and soon collapsing. Later on the DW transitions regularly and temporarily to regime III, with a frequency increasing with the magnitude of the current. We believe that the dynamical equilibrium of regime II and the prevention of a full Walker process in regime III result from an exchange-spring effect with the axial core, preventing the process to reach the axis of the wire. Thus, overall the DW speed remains high.

FIG. 4b illustrates DW motion over time and its three regimes. Note that all of the above has been simulated for DW propagation direction parallel to the axial vector for domain circulation on either side, be it for positive or negative (Ersted field: $C+$ on the right-hand side and $C-$ on the left-hand side (dotted line in FIG. 4b). While regimes I and II occur similarly for DW propagation antiparallel to the axial vector for domain circulation on either side, there is a drastic difference for regime III, which remains indefinite with a very low speed (dotted line in FIG. 4b). We believe that this dramatic non-reciprocity effect is induced by curvature, analogous to that of spin-wave propagation[45, 46]. Both spin-wave and DW motion indeed share the Damon-Eshbach geometry[47] with propagation direction and peripheral magnetization \mathbf{M} perpendicular. Non-reciprocal effects of DW motion due to curvature have been reported, *e.g.*, in twisted ribbons[48]. However, note that the time for the first transition to regime III is a few nanoseconds, *i.e.*, longer than the experimental pulse length. We therefore expect that regime III may not be relevant in the present experiments, explaining the absence of non-reciprocity (FIG. 2b). Nevertheless, the apparent experimental speed is 2 to 3 times larger than the simulated one. Further simulations is needed to fully explain this discrepancy, provide more details about the different dynamic regimes, and the microscopic understanding of the non-reciprocal effect probably deserve more extensive simulations. Intrinsic (*e.g.*, strength of spatial profile of anisotropy) or extrinsic (*e.g.*, granular structure) effects may also contribute to further delaying the Walker breakdown.

IV. CONCLUSION

We have measured unexpectedly-fast Ersted-field-driven domain wall motion in cylindrical nanowires with azimuthal peripheral magnetization ($\approx 600 \text{ m/s}$). Micromagnetic simulations reveal that several domain-wall transformations occur up to the onset of a Walker process, involving surface vortices/antivortices and Bloch points in the sub-surface area. However this process remains localized at the wire periphery and soon collapses, preserving the high DW mobility, and is also

non-reciprocal depending on the set of two domain circulations on either side of a given DW. Both effects are specific to three-dimensional nanomagnetism, in which a topology-locked exchange-spring effect between the peripheral and the core magnetization prevents the Walker breakdown, and curvature induces non-reciprocity. As such, it is expected to be specific to nanowires with radius of the order of 100 nm, for which exchange energy is sizable.

V. ACKNOWLEDGMENTS

We thank L. Vila, W. Saverio Torres and K. Garello for assistance with the magnetoresistance measurements. We acknowledge support from the team of the Nanofab platform (Institut Néel) and the French RENATECH network implemented at the Upstream Technological Platform in Grenoble PTA (ANR-22-PEEL-0015). The work was partially supported by Projects PID2023-150853NB-C31, PID2024-155385NB-C31 and PID2024-155385NA-C32, funded by MICIU/AEI /10.13039/501100011033 and by FEDER, UE and by Comunidad de Madrid via grant TEC-2024/TEC-380 (Mag4TIC-CM), and the QuantAlps Labex in Grenoble. A CC-BY public copyright license has been applied by the authors to the present document and will be applied to all subsequent versions up to the Author Accepted Manuscript arising from this submission, in accordance with the grant's open access conditions [49].

VI. END MATTER

A. Fabrication

Permalloy cylindrical nanowires of 200 nm diameter with compositional modulations along their length were synthesized by template-assisted electrochemical deposition. Nanoporous anodic aluminium oxide (AAO) templates were prepared by one-step hard anodization of Al disks with the pores opened to a final diameter of 200 nm[50]. Electrodeposition was carried out under conditions similar to those described in [19], using an electrolyte composed of NiSO₄ (0.47 M), NiCl₂ (0.01 M), FeSO₄ (0.09 M) and H₃BO₃ (0.4 M). Applied voltage pulses of -1.35 V during 200 s led to the deposition of permalloy (Fe₂₀Ni₈₀) segments with a length of 3.6 μ m, while short pulses of -1.1 V for 20 s allowed the deposition of chemical modulations with a composition of Fe₇₀Ni₃₀, 40 nm to 60 nm in length.

After growth, the nanowires were released from the template and dispersed on a Si substrate with 40 nm-thick Si₃N₄ windows to allow X-ray transmission for TXM and STXM/ptychography experiments. Two Au/Ti contact pads were made in each nanowire with laser lithography. The Si chip was then mounted on a dedicated printed cardboard (PCB) equipped with SMP

connectors, which were connected with a flexible cable to an SMP/SMA port of the microscope vacuum vessel. The two electric pads were connected to the PCB with microbonding. Based on the two-point resistances measured, the geometry of the wires (diameter and distance between the two contacts) and neglecting the resistance of the leads, the resistivity of the wires was $\rho = 2.8 \times 10^{-7} \Omega \cdot \text{m}$ with a low dispersion from wire to wire. This is similar to the bulk value, around $\rho = 2 \times 10^{-7} \Omega \cdot \text{m}$ at room temperature[51], and lower than permalloy in physical vapor deposition thin films, around $5 \times 10^{-7} \Omega \cdot \text{m}$ to $6 \times 10^{-7} \Omega \cdot \text{m}$ for films 100 nm and thicker[52, 53].

B. Transmission X-ray Microscopy and Ptychography

XMCD measurements were performed either at the MISTRAL beamline in ALBA synchrotron using a transmission X-ray microscope (TXM) in static conditions, or at the HERMES beamline in SOLEIL synchrotron using ptychography, in static or time-resolved conditions.

TXM at MISTRAL uses a glass capillary to focus the beam on the sample field of view, and a zone plate to construct the image and record it with a camera. TXM has a spatial resolution of about 25 nm. The photon energy was tuned to the Fe L₃ absorption edge.

Ptychography is an extension of scanning transmission X-ray microscopy (STXM), recording far-field diffraction patterns for overlapping 2D rastered-scanned points on the sample, with a probe size ≈ 50 nm. An iterative algorithm allows to reconstruct both the intensity and the phase of X-rays at every location of the sample, with a spatial resolution around 10 nm. When combined with XMCD, ptychography provides information about the component of magnetization parallel to the X-ray beam. We set the X-ray energy around 1 eV below the Fe L₃ edge, which decreases absorption while maintaining a significant magnetic scattering, suitable to image thick samples as in the present case[54]. To obtain time resolution, an oscillatory ac current was fed inside the wire at the cavity radio frequency of the ring, 352.202 MHz, and synchronized with the clock signal from the synchrotron. Consequently, in the case of reproducible magnetic processes, every X-ray bunch probes the same distribution of magnetization. Adjusting the time delay between pump and probe over one period allows one to build a magnetic video of the magnetization process. More details of the technique will be published elsewhere.

C. Electric current pulses

In this section, we present the method used to determine the duration of the experimental current pulses and the role of Joule heating. We use a 100 MHz oscilloscope to monitor two pulses of current: first, after the

pulse generator and before sample, using a $M\Omega$ load, and second, after the sample, using a 50Ω load. The latter allows to determine the current flowing through the sample, while a significant part of the pulse is reflected due to the resistance mismatch with the sample. We checked that the sample resistance inferred either from a dc measurement with a multimeter, or from the height of pulses sent, reflected and transmitted, match together.

The pulse length was determined from the injected current pulses using current-density thresholds. Since the data in FIG. 2 is based on the initial nucleation of a domain, we define that the pulse begins when the measured voltage corresponds to the minimum current density required for domain nucleation $1.1 \times 10^{11} \text{ A/m}^2$. Similarly, we define that the pulse ends at the minimum current density allowing DW motion $2.51 \times 10^{10} \text{ A/m}^2$. These two values were obtained from the experimental results shown in Figure 5(a,b). To determine the error bars, the upper bound of the pulse length was considered to be the total length of the measured pulse, while the lower bound corresponds to the length of the plateau. The upper and lower bounds and the effective pulse length are represented in Figure 5(c,d).

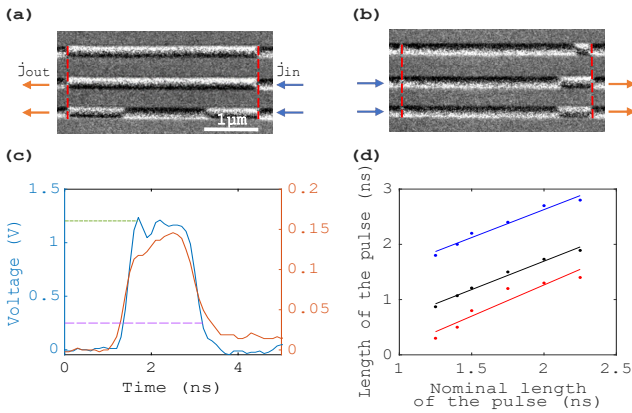


FIG. 5: (a,b) The top TXM images show initial states.

The following images in each sequence are after applying current pulses to the initial state of (a) 1.04×10^{11} and $1.1 \times 10^{11} \text{ A/m}^2$ and (b) 2.2×10^{10} and $6.9 \times 10^9 \text{ A/m}^2$, respectively. (c) Injected (blue) and transmitted (orange) pulse shape for a pulse with nominal voltage 1.2 V. The green and purple dashed lines correspond to the minimum injected voltage of the incoming pulse required for DW nucleation and motion, respectively. (d) Upper (blue) and lower (red) bounds, and the effective experimental (black) length of the pulse measured after the sample, versus the nominal length, and their corresponding linear fits.

An upper bound of the increase of temperature ΔT due to Joule heating in a nanowire can be calculated as:

$$\Delta T = \frac{j^2 \rho t}{Dc} \quad (4)$$

where j and t are the current density and duration of

the electric pulses and ρ , D , c are the resistivity, density, and the specific heat capacity per unit mass of the nanowire, respectively. For the case of a 240 nm-diameter permalloy nanowire, we use our experimentally measured value of $\rho = 2.8 \times 10^{-7} \Omega \cdot \text{m}$ and literature values for $c = 1.1 \text{ J/(g} \cdot \text{K)}$ for Ni nanowires, and bulk density $D = 8.6 \text{ g/m}^3$. For the maximum length of the current pulse, 2.25 ns, and a current density of $j = 1.1 \times 10^{11} \text{ A/m}^2$, we estimate a maximum increase of temperature of 0.8 K. Hence, we consider Joule heating to be negligible in the study of domain wall motion under current pulses in this system. This arises thanks to the low current density, good electrical conductivity of the material, short pulse length and single-pulse usage.

D. Coherent switching for large current density

Converting the DW position measured between two current pulses into DW speed, requires that the underlying mechanism is indeed DW motion. A sanity check is that the inferred speed is largely independent of the pulse length, which is the protocol used in the manuscript. Using time-resolved ptychography imaging, we checked that DW motion is indeed the mechanism at low-enough current density, while coherent reversal can occur at large current (FIG. 6,) which can lead to unrealistically-large values of DW speed if interpreted as DW motion. In this experiment, a permalloy nanowire with similar characteristics was investigated under low- and high-current AC excitation. We believe that the difference of threshold for DW motion and coherent reversal, compared to the wires images with TXM, result from difference in the magnitude of magnetic anisotropy.

E. Evaluation of the value of magnetic anisotropy

In the micromagnetic simulations, the azimuthal state was promoted by considering a hard-axis contribution to magnetic anisotropy K_u . We evaluated the strength of K_u by comparing anisotropic magnetoresistance (AMR) measurements of an electrically-contacted individual nanowire, with TetraX micromagnetic simulations.

AMR was measured while applying a magnetic field successively perpendicular and parallel to the wire axis, up to a magnitude sufficient to reach a saturation state. Resistance is larger for magnetization parallel with the current, as usual for Permalloy. By comparing the value of resistances for saturation along the two directions, we determined the magnitude of AMR to be $\Delta_{\text{AMR}} \approx 3\%$. Note that in the rare cases that a contact resistance adds up, the total resistance is increased and the apparent AMR is decreased. From the apparent AMR, we defined the normalized resistance $\rho = 1 - (R_{\parallel} - R)/(R_{\parallel} \cdot \Delta_{\text{AMR}})$, which we show versus magnetic field applied parallel to the nanowire axis on FIG. 7a. The high resistance

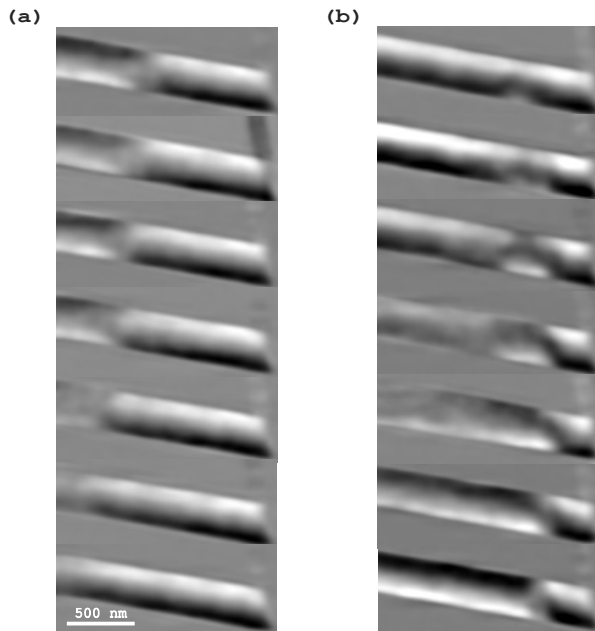


FIG. 6: Time-resolved ptychography images. The nanowire was excited with an AC current at 352.202 MHz and a current density of (a) 3×10^{10} A/m² and (b) 4.9×10^{10} A/m². Frames were acquired every 240 ps.

level reached under a few tens of mT is associated to magnetization saturation along the axial direction, while the lower values of resistance around remanence result from the curling of magnetization at the periphery of the wire. Similar to the micromagnetic simulations reported in the main text, we considered a 200 nm-diameter permalloy disk, with $M_s = 800 \times 10^3$ A/m and $A_{\text{ex}} = 13 \times 10^{-12}$ J/m. The resulting AMR was computed from the cross-sectional average $\langle m_z^2 \rangle$. The magnitude of the uniaxial anisotropy K_u was varied systematically. The comparison between the experimental and simulated AMR curves is not straightforward due to the hysteresis, which is larger in the micromagnetic simulation, considering an infinite and translational-invariant wire. In the experimental case, the hysteresis associated with the switching of circulation can be promoted the wire ends, chemical modulations and the existence of domains. We therefore focused the comparison on the first part of the loops, from saturation to remanence and only slightly

beyond. By comparing different experimental measurements with the set of simulated curves, we estimate an anisotropy in the range $K_u = 6 \times 10^3$ J/m³ to 10^4 J/m³. We subsequently used the latter in the micromagnetic simulations presented in the manuscript, as it better fits the details of the magnetic configuration of the domain wall (FIG. 3f-g).

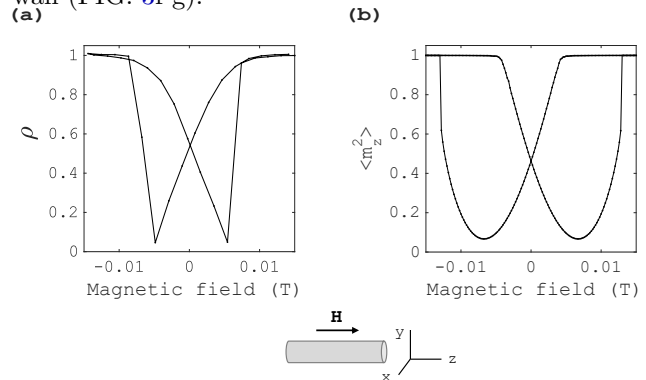


FIG. 7: (a) Normalized experimental AMR curve of a 240 nm permalloy nanowire with magnetic field parallel to the axis. (b) Simulated $\langle m_z^2 \rangle$ versus magnetic field applied parallel to the axis for $K_u = 6 \times 10^3$ J/m³.

F. Micromagnetic simulations

Material parameters are identical in *feLLGood* and *MuMax*: magnetization $M_s = 800$ kA/m, exchange stiffness $A_{\text{ex}} = 13 \times 10^{12}$ J/m, hard-axis uniaxial anisotropy $K_u = 10^4$ J/m³, gyromagnetic ratio $\gamma = 1.7595 \times 10^{11}$ T/m. The volume of the cells is 8 nm^3 cubic cells for *MuMax*, 8.6 nm^3 tetrahedra on the average for *feLLGood*, meshed with *Gmsh*[55] using an extrusion method along the axis of the wire.

The time-dependent position of the DW in *MuMax* simulations was determined from the spatial distribution of the longitudinal component of magnetization m_z at the periphery of the wire. For each time step, we consider two cross-sections parallel to the wire axis, one near the upper and one near the lower edges of the nanowire. Along each, we determined the minimum value of the azimuthal component, which identifies the position of the DW. Because the DW is not rotationally-invariant, these two values may be slightly different. To minimize this effect, the DW position was computed as the average of these two values.

-
- [1] A. Thiaville and Y. Nakatani, *Spin dynamics in confined magnetic structures III* (Springer, Berlin, 2006) Chap. Domain-wall dynamics in nanowires and nanostrips, pp. 161–205.
- [2] A. Thiaville and Y. Nakatani, *Nanomagnetism and spintronics* (Elsevier, 2009) Chap. Micromagnetic simulation

- of domain wall dynamics in nanostrips, pp. 231–276.
- [3] L. Thomas and S. S. P. Parkin, *Micromagnetism* (Wiley, Chichester, England, 2007) Chap. Current induced domain-wall motion in magnetic nanowires, pp. 942–982.
- [4] A. Mougin, M. C. and J.P. Adam, P. Metaxas, and J. Ferré, *Domain wall mobility, stability and walker break-*

- down in magnetic nanowires, *Europhys. Lett.* **78**, 57007 (2007).
- [5] G. S. D. Beach, C. Nistor, C. Knuston, M. Tsoi, and J. L. Erskine, *Dynamics of field-driven domain-wall propagation in ferromagnetic nanowires*, *Nat. Mater.* **4**, 741 (2005).
- [6] M. Hayashi, L. Thomas, C. Rettner, R. Moriya, Y. B. Bazaliy, and S. S. P. Parkin, *Current driven domain wall velocities exceeding the spin angular momentum transfer rate in permalloy nanowires*, *Phys. Rev. Lett.* **98**, 037204 (2007).
- [7] M. Hayashi, L. Thomas, C. Rettner, R. Moriya, and S. S. P. Parkin, *Direct observation of the coherent precession of magnetic domain walls propagating along permalloy nanowires*, *Nat. Phys.* **3**, 21 (2007).
- [8] A. Thiaville, S. Rohart, E. Jué, V. Cros, and A. Fert, *Dynamics of Dzyaloshinskii domain walls in ultrathin magnetic films*, *Europhys. Lett.* **100**, 57002 (2012).
- [9] K.-J. Kim, S. K. Kim, Y. Hirata, S.-H. Oh, T. Tono, D.-H. Kim, T. Okuno, W. S. Ham, S. Kim, G. Go, Y. Tserkovnyak, A. Tsukamoto, T. Moriyama, K.-J. Lee, and T. Ono, *Fast domain wall motion in the vicinity of the angular momentum compensation temperature of ferrimagnets*, *Nat. Mater.* **16**, 1187 (2017).
- [10] L. Caretta, M. Mann, F. Büttner, K. Ueda, B. Pfau, C. M. Günther, P. Hensing, A. Churikova, C. Klose, M. Schneider, D. Engel, C. Marcus, D. Bono, K. Bagschik, S. Eisebitt, and G. S. D. Beach, *Fast current-driven domain walls and small skyrmions in a compensated ferrimagnet*, *Nat. Nanotechnol.* **13**, 1154 (2018).
- [11] A. Fernandez-Pacheco, R. Streubel, O. Fruchart, R. Hertel, P. Fischer, and R. P. Cowburn, *Three-dimensional magnetism*, *Nat. Commun.* **8**, 15756 (2017).
- [12] R. Streubel, E. Y. Tsymbal, and P. Fischer, *Magnetism in curved geometries*, *J. Appl. Phys.* **129**, 210902 (2021).
- [13] D. Makarov and D. Sheka, eds., *Curvilinear Micromagnetism: From Fundamentals to Applications* (Springer International Publishing, 2022).
- [14] O. V. Pylypovskiy, V. P. Kravchuk, D. D. Sheka, D. Makarov, O. G. Schmidt, and Y. Gaididei, *Coupling of chiralities in spin and physical spaces: The möbius ring as a case study*, *Phys. Rev. Lett.* **114**, 197204 (2015).
- [15] R. Hertel, *Ultrafast domain wall dynamics in magnetic nanotubes and nanowires*, *J. Phys.: Condens. Matter* **28**, 483002 (2016).
- [16] M. Yan, C. Andreas, A. Kakay, F. Garcia-Sanchez, and R. Hertel, *Fast domain wall dynamics in magnetic nanotubes: Suppression of Walker breakdown and Cherenkov-like spin wave emission*, *Appl. Phys. Lett.* **99**, 122505 (2011).
- [17] M. Schöbitz, A. De Riz, S. Martin, S. Bochmann, C. Thirion, J. Vogel, M. Foerster, L. Aballe, T. O. Menteş, A. Locatelli, F. Genuzio, S. Le Denmat, L. Cagnon, J. Toussaint, D. Gusakova, J. Bachmann, and O. Fruchart, *Fast domain walls governed by topology and astatic fields in cylindrical magnetic nanowires*, *Phys. Rev. Lett.* **123**, 217201 (2019).
- [18] C. Bran, J. A. Fernandez-Roldan, J. A. Moreno, A. F. Rodríguez, R. P. del Real, A. Asenjo, E. Saugar, J. Marqués-Marchán, H. Mohammed, M. Foerster, L. Aballe, J. Kosel, M. Vazquez, and O. Chubykalo-Fesenko, *Domain wall propagation and pinning induced by current pulses in cylindrical modulated nanowires*, *Nanoscale* **18**, 8387 (2022), arXiv:2210.01480 [cond-mat.mtrl-sci].
- [19] S. Ruiz-Gómez, M. Foerster, L. Aballe, M. P. Proenca, I. Lucas, J. L. Prieto, A. Mascaraque, J. de la Figuera, A. Quesada, and L. Pérez, *Observation of a topologically protected state in a magnetic domain wall stabilized by a ferromagnetic chemical barrier*, *Sci. Rep.* **8**, 16695 (2018).
- [20] J. A. Fernandez-Roldan, C. Bran, A. Asenjo, M. Vázquez, A. Sorrentino, S. Ferrer, O. Chubykalo-Fesenko, and R. P. del Real, *Spatial magnetic imaging of non-axially symmetric vortex domains in cylindrical nanowire by transmission x-ray microscopy*, *Nanoscale* **14**, 13661 (2022).
- [21] R. Coehoorn, D. B. de Mooij, J. P. W. B. Duchateau, and L. H. J. Buschow, *Novel permanent magnetic materials by rapid quenching*, *J. Phys.* **49** C-8, 10.1051/jphyscol:19888304 (1988).
- [22] E. F. Kneller, *The exchange-spring magnet: a new material principle for permanent magnets*, *IEEE Trans. Magn.* **27**, 3588 (1991).
- [23] R. Skomski and J. M. D. Coey, *Giant energy product in nanostructured two-phase magnets*, *Phys. Rev. B* **48**, 15812 (1993).
- [24] J. Stöhr, H. A. Padmore, S. Anders, T. Stammler, and M. R. Scheinfein, *Principles of x-ray magnetic dichroism spectromicroscopy*, *Surf. Rev. Lett.* **05**, 1297 (1998).
- [25] K. Bushida, M. Noda, L. Panina, H. Yoshida, T. Uchiyama, and K. Mohri, *Magneto-impedance element using amorphous micro wire*, *IEEE Trans. J. Magn. Jap.* **9**, 7 (1994).
- [26] L. V. Panina and K. Mohri, *Magneto-impedance effect in amorphous wires*, *Applied Physics Letters* **65**, 1189 (1994).
- [27] A. Chizhik, J. Gonzalez, A. Zhukov, and J. M. Blanco, *Circular magnetic bistability in co-rich amorphous microwires*, *J. Phys. D: Appl. Phys.* **36**, 419 (2003).
- [28] A. Chizhik, A. Zhukov, A. Stupakiewicz, A. Maziewski, J. Blanco, and J. Gonzalez, *Kerr microscopy study of magnetic domain structure changes in amorphous microwires*, *IEEE Trans. Magn.* **45**, 4279 (2009).
- [29] V. Zhukova, J. M. Blanco, A. Chizhik, M. Ipatov, and A. Zhukov, *Ac-current-induced magnetization switching in amorphous microwires*, *Front. Phys.* **13**, 10.1007/s11467-017-0722-6 (2018).
- [30] S. Jamet, N. Rougemaille, J. C. Toussaint, and O. Fruchart, *Magnetic nano- and microwires: Design, synthesis, properties and applications* (Woodhead, 2015) Chap. Head-to-head domain walls in one-dimensional nanostructures: an extended phase diagram ranging from strips to cylindrical wires, pp. 783–811.
- [31] M. Kuepferling, A. Casiraghi, G. Soares, G. Durin, F. Garcia-Sanchez, L. Chen, C. Back, C. Marrows, S. Tacchi, and G. Carlotti, *Measuring interfacial dzyaloshinskii-moriya interaction in ultrathin magnetic films*, *Reviews of Modern Physics* **95**, 015003 (2023).
- [32] (), <http://feellgood.neel.cnrs.fr><http://feellgood.neel.cnrs.fr>.
- [33] A. Vansteenkiste, J. Leliaert, M. Dvornik, M. Helsen, F. Garcia-Sanchez, and B. V. Waeyenberge, *The design and verification of MuMax3*, *AIP Advances* **4**, 107133 (2014).
- [34] A. E. LaBonte, *Two-dimensional bloch-type domain walls in ferromagnetic thin films*, *J. Appl. Phys.* **40**, 2450 (1969).

- [35] A. Hubert, *Stray-field-free magnetization configurations*, Phys. Stat. Sol. **32**, 519 (1969).
- [36] S. Jamet, S. D. Col, N. Rougemaille, A. Wartelle, A. Locatelli, T. O. Menteş, B. S. Burgos, R. Afid, L. Cagnon, J. Bachmann, S. Bochmann, O. Fruchart, , and J. C. Toussaint, *Quantitative analysis of shadow x-ray magnetic circular dichroism photo-emission electron microscopy*, Phys. Rev. B **92**, 144428 (2015).
- [37] J. Hurst, A. De Riz, M. Staño, J.-C. Toussaint, O. Fruchart, and D. Gusakova, *Theoretical study of current-induced domain wall motion in magnetic nanotubes with azimuthal domains*, Phys. Rev. B **103**, 024434 (2021).
- [38] A. Wartelle, B. Trapp, M. Staño, C. Thirion, S. Bochmann, J. Bachmann, M. Foerster, L. Aballe, T. O. Menteş, A. Locatelli, A. Sala, L. Cagnon, J. Toussaint, and O. Fruchart, *Bloch-point-mediated topological transformations of magnetic domain walls in cylindrical nanowires*, Phys. Rev. B **99**, 024433 (2019), arXiv:1806.10918.
- [39] A. De Riz, J. Hurst, M. Schöbitz, C. Thirion, J. Bachmann, J. C. Toussaint, O. Fruchart, and D. Gusakova, *Mechanism of fast domain wall motion via current-assisted bloch-point domain wall stabilization*, Phys. Rev. B **103**, 054430 (2021).
- [40] L. Álvaro Gómez, J. Hurst, S. Hegde, S. Ruiz-Gómez, E. Pereiro, L. Aballe, J. C. Toussaint, L. Pérez, A. Masseboeuf, C. Thirion, O. Fruchart, and D. Gusakova, *Topological analysis and experimental control of transformations of domain walls in magnetic cylindrical nanowires*, Phys. Rev. Research **7**, 023092 (2025).
- [41] B. Van Waeyenberge, A. Puzic, H. Stoll, K. W. Chou, T. Tylliszczak, R. Hertel, M. Fähnle, H. Brückl, K. Rott, G. Reiss, I. Neudecker, D. Weiss, C. H. Back, and G. Schütz, *Magnetic vortex core reversal by excitation with short bursts of an alternating field*, Nature **444**, 461 (2006).
- [42] R. Hertel, S. Gliga, M. Fähnle, and C. M. Schneider, *Nanomagnetic toggle switching of vortex cores on the picosecond time scale*, Phys. Rev. Lett. **98**, 117201 (2007).
- [43] K. Yamada, S. Kasai, Y. Nakatani, K. Kobayashi, H. Kohno, A. Thiaville, and T. Ono, *Electrical switching of the vortex core in a magnetic disk*, Nat. Mater. **6**, 270 (2007).
- [44] Y. Nakatani, A. Thiaville, and J. Miltat, *Head-to-head domain walls in soft nano-strips: a refined phase diagram*, J. Magn. Magn. Mater. **290-291**, 750 (2005).
- [45] J. A. Otálora, M. Yan, H. Schultheiss, R. Hertel, and A. Kákay, *Curvature-induced asymmetric spin-wave dispersion*, Phys. Rev. Lett. **117**, 227203 (2016).
- [46] J. A. Otálora, M. Yan, H. Schultheiss, R. Hertel, and A. Kákay, *Asymmetric spin-wave dispersion in ferromagnetic nanotubes induced by surface curvature*, Phys. Rev. B **95**, 184415 (2017).
- [47] D. D. Stancil and A. Prabhakar, *Spin waves. Theory and applications* (Springer, New-York, 2009).
- [48] A. M. A. Farinha, S.-H. Yang, J. Yoon, B. Pal, and S. S. P. Parkin, *Interplay of geometrical and spin chiralities in 3d twisted magnetic ribbons*, Nature **639**, 67 (2025).
- [49] (), <https://creativecommons.org/licenses/by/4.0/>.
- [50] A. Domínguez-Bajo, J. M. Rosa, A. González-Mayorga, B. L. Rodilla, A. Arché-Núñez, E. Benayas, P. Ocón, L. Pérez, J. Camarero, R. Miranda, M. T. González, J. Aguilar, E. López-Dolado, and M. C. Serrano, *Nanostructured gold electrodes promote neural maturation and network connectivity*, Biomaterials **279**, 121186 (2021).
- [51] G. Couderchon and J. L. Porteseil, *The iron-nickel alloys* (Lavoisier, 1996) Chap. Some properties of nickel-rich commercial Fe-Ni alloys, p. 27.
- [52] J. Lo, C. Hwang, T. C. Huang, R. Campbell, and D. Allee, *Magnetic and structural properties of high rate dual ion-beam sputtered nife films (invited)*, Journal of Applied Physics **61**, 3520 (1987).
- [53] G. Counil, T. Devolder, J.-V. Kim, P. Crozat, C. Chappert, S. Zoll, and R. Fournel, *Temperature dependences of the resistivity and the ferromagnetic resonance linewidth in permalloy thin films*, IEEE Trans. Magn. **42**, 3323 (2006).
- [54] C. Donnelly, V. Scagnoli, M. Guizar-Sicairos, M. Holler, F. Wilhelm, F. Guillou, A. Rogalev, C. Detlefs, A. Menzel, J. Raabe, and L. J. Heyderman, *High-resolution hard x-ray magnetic imaging with dichroic ptychography*, Phys. Rev. B **94**, 064421 (2016).
- [55] C. Geuzaine and J. Remacle, *Gmsh: A 3-d finite element mesh generator with built-in pre- and post-processing facilities*, Int. J. Num. Meth. Engineer. **79**, 1309 (2009).